UNIVERSITY OF TURKU

Monitoring laser welding via coaxial imaging

Department of Mechanical and Materials Engineering

Bachelor's thesis

Author:

Olli Ranto

27.4.2026

Turku

Kandidaatintutkielma

Tutkinto-ohjelma, oppiaine: Konetekniikka

Tekijä(t): Olli Ranto

Otsikko: Monitoring laser welding via coaxial imaging

Ohjaaja(t): Li-Wei Hsu

Sivumäärä: 27 sivua

Päivämäärä: 27.4.2026

Tiivistelmä

Avaimenreiän vakaus on merkittävin haaste avaimenreikälaserhitsauksessa. Epävakaa avaimenreikä on keskeinen syy hitsausvirheisiin, kuten huokosiin ja roiskeisiin. Nämä virheet heikentävät hitsin eheyttä ja johtavat epäluotettaviin liitoksiin. Perinteisiä rikkomattomia aineenkoetusmenetelmiä (NDT) voidaan käyttää virheiden havaitsemiseen, mutta ne vaativat lisätyötä. Hitsausprosessin valvonta voisi mahdollisesti poistaa NDT:n tarpeen; avaimenreikää voitaisiin valvoa suoraan. Tässä opinnäytetyössä esitetään uusi menetelmä avaimenreiän vakauden valvontaan: avaimenreiän ääriviivat erotetaan koaksiaalisesta kuvamateriaalista, ja aineistosta lasketaan keskihajonta kuvaamaan avaimenreiän muodon muutosten suuruutta. Konvoluutioneuroverkko (CNN), joka perustuu U-net-arkkitehtuuriin, koulutettiin segmentoimaan avaimenreikä semanttisesti hitsausprosessin kuvista. Tehon vaikutusta keskihajontaan tutkittiin, ja tämän menetelmän avulla havaittiin, että avaimenreikä on vakaampi, kun hitsataan lähellä optimaalisia parametreja.

Avainsanat: Avaimenreiän semanttinen segmentointi, U-net, Avaimenreiän vakauden valvonta

Bachelor's thesis

Subject: Mechanical engineering

Author(s): Olli Ranto

Title: Monitoring laser welding via coaxial imaging

Supervisor(s): Li-Wei Hsu

Number of pages: 27 pages

Date: 27.4.2026

Abstract

The keyhole stability is a significant challenge in keyhole laser welding. An unstable keyhole is the main contributor to welding defects, such as pores and spatter. The welding defects compromise the weld integrity, leading to unreliable joints. Traditional non-destructive testing (NDT) methods can be used to detect welding defects, but require extra work. Welding process monitoring could possibly eliminate the need for NDT by directly monitoring the keyhole. This thesis proposes a novel method of monitoring keyhole stability: the keyhole contours are extracted from coaxial footage, and the standard deviation is calculated from the data to represent the magnitude of change in the shape of the keyhole. A convolutional neural network (CNN) with the U-net architecture was trained to semantically segment the keyhole from the welding process images. The effect of power on the standard deviation was studied; using this method, it was found that the keyhole is more stable when welding near the optimal parameters.

Keywords: Semantic segmentation of a keyhole, U-net, Keyhole stability monitoring

Use of artificial intelligence in thesis

Artificial intelligence was used for the following tasks:

- **Coding** — Most of the code was created using either Chatgpt 5.3 or Deepseek 3.2.
- **Proofreading** — The Writefull AI integrated with Overleaf was used for proofreading.

I acknowledge that I am fully responsible for the entire content of my thesis, including the parts generated by AI, and accept accountability for any violations of ethical standards in publications.

Contents

1 Introduction

The interest in laser welding has risen significantly over the years. Laser welding offers significant benefits over traditional welding methods, such as high power density, a small heat affected zone (HAZ), deep penetration, and high speed [1]. In addition, the cost of laser welding equipment has decreased in recent years, largely driven by increased competition in the global laser equipment manufacturing market. The growing maturity and large-scale production capabilities of laser manufacturing technologies — particularly in countries such as China — have further contributed to this trend.

However, laser welding certain materials, such as aluminium and thick materials, still presents major challenges with the stability of the keyhole. An unstable keyhole is prone to forming welding defects, such as pores and spatter [2]. To ensure the laser weld is defect free, multiple monitoring methods have been proposed. The laser welding process monitoring can be substantially more cost effective compared to post-process weld testing, such as radiographic testing, due to the reduction in labor.

One of the cheapest monitoring methods, and the main topic of this thesis, is coaxial camera monitoring. Laser welding heads often feature a camera port, making coaxial camera monitoring easy to implement. The major problem with current coaxial monitoring methods is that there is no commercial software available to process the data from the footage. Therefore, the implementation of a coaxial camera monitoring system requires extensive research on defect detection from the footage. The success of a coaxial monitoring system depends on two factors: The image quality and the image processing algorithms.

Many current studies on coaxial monitoring have used traditional machine vision algorithms, such as edge detection, to detect keyhole contours. The key advantages of a traditional machine vision algorithm are low computing power requirements and simplicity. Simplicity often comes with limitations in adaptability. Traditional methods often struggle to handle variability in imaging conditions, such as changes in exposure or lighting. Under well-controlled and consistent conditions, traditional algorithms can even outperform deep-learning-based approaches in accuracy. To better handle varying conditions, deep-learning-based machine vision algorithms can be employed. The downside is that training such a model requires large amounts of data.

The number of training images required depends on the convolutional neural network (CNN) architecture. The chosen model, the U-net, typically requires fewer training images compared to standard CNNs like ResNet. The U-net CNN was first proposed by [3] Ronneberger et al. for biomedical segmentation. The U-net was designed to work with a scarce amount of data due to the lack of biomedical data. For laser welding, it is easy to collect thousands of images from the coaxial camera, but each image in the training dataset requires an annotation mask. In the initial stages of training the model, the annotation masks often have to be hand drawn.

To reduce the manual labor needed for annotating the masks, methods such as pseudo-labeling can be used. The pseudo-labeling was first proposed by Lee [4] as a semi-supervised learning method for neural networks. Pseudo-labeling allows the model to be trained with both labeled and unlabeled data; the CNN, trained first with labeled data, is used to create pseudo-labels for the unlabeled images. It was proven by Lee [4] that by using pseudo-labels, the model can achieve better generalization performance.

This thesis aims to study how to quantify keyhole stability. A U-net was trained to semantically segment the contours of the keyhole. The U-net architecture was chosen for its high segmentation accuracy and low data quantity requirements. Data were collected from the contours, and the standard deviation was calculated from the data. The magnitude of the standard deviation represents how much the keyhole contours change. A high standard deviation would suggest a lot of change in the shape of the keyhole, indicating unstable keyhole behavior. A low standard deviation would suggest the opposite: a stable keyhole.

2 Laser welding monitoring

There are multiple ways to monitor a laser welding process. Over the years, multiple monitoring methods have been proposed, such as acoustic emission monitoring (AE), optical coherence tomography (OCT), infrared (IR) thermography/pyrometry, and both coaxial and off-axis camera monitoring. This thesis focuses on coaxial camera monitoring.

2.1 Keyhole stability

During laser welding, a vapor capillary called a keyhole is formed; the high intensity laser beam vaporizes the metal workpiece, producing a keyhole. Both keyhole and melt pool dynamics are assumed to be the main contributors to weld defects such as spatter and pores. The instabilities of the highly dynamic keyhole and melt pool are assumed to be caused by fluctuations in the laser intensity distribution within the keyhole. The changes in laser intensity distribution are caused by changes in laser energy absorption, which are proportional to the beam reflections in the keyhole. [2]

When the Laser beam hits a metal workpiece, it is partially reflected and partially absorbed. The absorbed beam melts and vaporizes the metal target, forming the keyhole. The rapid formation of the vapor creates a pressure that keeps the keyhole open and is referred to as the recoil pressure. The laser beam energy is absorbed by both Fresnel absorption, which is the energy absorbed directly from the beam to the metal workpiece, and metal vapor absorption, which is the energy absorbed by the vapor. The nearly vertical walls of the keyhole cause multiple laser beam reflections within the keyhole that efficiently transfer the energy from the laser beam to the workpiece. [2]

The movement of the laser beam during welding leads to a nonuniform distribution of laser intensity; the laser beam moves toward the front wall of the keyhole, causing the highest intensity beam to land on the front wall of the keyhole. Also, Because of the movement, the keyhole lags behind the beam [5]. The bottom of the keyhole lags behind the beam the most, creating a keyhole that is tilted or curved towards the rear wall [6]. The front wall of the keyhole is rather solid, with only a thin layer of molten metal, unlike the rear wall, which is the melt pool. Metal vaporizes from the front wall of the keyhole, but due to the rigidity of the front wall, the pressurized jet of metal vapor is directed towards the molten rear wall [1]. The pressurized jet is strongest near

the bottom of the keyhole due to the keyhole being tilted towards the rear wall. The pressurized jet and the recoil pressure at the bottom widen the bottom of the keyhole towards the rear [2], which can cause the melt pool to bulge towards the keyhole. The bulging can cause the keyhole to collapse, trapping gas in the melt pool, leading to porosity [7].

As mentioned, the highest intensity laser beam lands on the front wall of the keyhole. This creates the highest recoil pressure on the front surface of the keyhole, causing a pressure gradient between the front and rear of the keyhole. The pressure gradient accelerates the molten metal around the keyhole. Spatter is formed when the melt attains enough momentum to leave the melt pool. Spatter can also be induced by metal vaporization within the keyhole; the resulting recoil pressure and high-velocity vapor flow exert shear stress on the keyhole walls, causing melt ejection. Additionally, low-boiling-point impurities can rapidly expand upon heating, producing jets that further contribute to melt ejection. [8]

2.2 Coaxial camera monitoring

An optical coaxial camera port is a common feature in laser welding heads. The camera port allows for easy integration of a CCD, CMOS, or SWIR camera to monitor the welding process. The camera view is parallel to the laser beam since it is coaxial. Multiple methods have been proposed for evaluating the penetration depth and defect formation of the keyhole from the coaxial footage. The methods mainly follow two trends: data extraction via measuring specified features of the keyhole, such as the shape and size, or via convolutional neural network (CNN) -based deep-learning algorithms.

The laser welding process emits intense light, which is often too bright for the camera sensor, producing over-saturated images. One way to achieve high quality welding process images is to equip the camera with a band-pass filter that only allows a specific wavelength of light to pass. In addition, external laser illumination with that specific wavelength is used to illuminate the welding process. The external illumination has to be more powerful than the filtered welding process light. This kind of setup allows the visualization of both the cold and hot regions simultaneously with minimal interference from the process light. [9]

Some studies [10, 11] have shown a very simple method of predicting laser weld penetration by detecting the presence of a full penetration hole in the coaxial footage. This approach may work

when welding thin metals because the full penetration hole might not be detectable while welding thick materials due to the keyhole being tilted towards the rear, which makes the penetration hole not visible to the camera.

Zhang et al.[12] proposed a method for monitoring penetration status and joint tracking using a high speed camera. The area of the keyhole and the area of the full penetration hole were extracted from the coaxial footage, and the ratio of the two was used to determine the penetration status. Additionally, the alignment between the keyhole and the joint was monitored to detect improper placement of the keyhole. It was found through experiments that the penetration status among incomplete penetration, moderate penetration, and over-penetration could be detected from the ratio of the areas.

Lu et al.[13] proposed a similar approach, but instead of evaluating the penetration status for each individual frame, the penetration status was determined for an interaction time. The interaction time was defined as the time the laser beam takes to move a distance equal to the diameter of the laser beam. The area of the keyhole, the area of the full penetration hole, and the frequency of detected full penetration holes were measured. The full penetration hole could not be detected in every frame, even if the penetration was sufficient; hence, the frequency was measured. The average and mean values of the areas over the interaction time were provided as input to a support vector machine. It was concluded that it is possible to determine the penetration status with a 96.5% classification accuracy by using multiple interaction time conditioned keyhole behaviors as inputs.

Ahmad et al. [14] extracted multiple features, such as area and roundness, from the keyhole geometry using machine vision. The weld was inspected using X-ray, and the pores detected with X-ray were matched with the corresponding coaxial images. The features extracted with coaxial imaging were combined with the pore data from X-ray imaging, and this data was used to train a machine learning algorithm. A strong correlation was found between porosity formation and fluctuations in roundness, Feret's diameter, and centroid position. A detection accuracy of about 80% was achieved.

Zhang et al. [15] trained a CNN model to detect pores during aluminum welding. The cross sections of the welded specimens were inspected, and pores were located and measured. The frames from the coaxial camera were labeled with porosity attributes, creating the training data. The

CNN model achieved a classification accuracy of 96.1%. A CNN with an automatic feature-learning capacity was utilized to achieve better accuracy than that of a model that uses defined features such as area and circularity.

A previously conducted experiment at the university of Turku by Núñez et al. [16] used pretrained CNNs to extract features from the coaxial images. The features were combined with penetration data collected by an inline coherent imaging system. The data were used to train a regression model to predict keyhole penetration. The model was able to predict the penetration with a 3% error.

2.3 Machine vision

The key to a successful coaxial monitoring system is the machine vision algorithm. The current state of machine vision can be divided into two categories: traditional and deep-learning-based machine vision [17]. Both have been shown to work for monitoring laser welding. Traditional feature extraction methods were used in studies [10, 11, 12, 13, 14], and the deep-learning-based in studies [15, 16]. This thesis mainly focuses on deep-learning-based machine vision using convolutional neural networks (CNNs).

CNNs are a combination of multiple layers, such as convolutional layers, pooling layers, and activation functions [17]. These layers are used to extract features from the image input. Convolutional layers are the main building blocks of CNNs. In a convolutional layer, the convolution is conducted by taking the dot product of the input and the kernel. A kernel is a small learnable matrix that is used to extract features from the input. The kernel is slid across the input while taking the dot product, creating the output feature map, as shown in Figure 1. The distance the kernel slides between each convolution operation is called a stride. Depending on the size of the kernel, the spatial size of the output feature map changes; the kernel outputs one value while requiring multiple inputs. If a 3x3 kernel size with a stride of one is used, each dimension of the feature map will be smaller by two compared to the input. This can be prevented by adding padding, meaning a row of zeros is added to each side of the feature map to maintain the spatial size. [18]

The convolution layer is often followed by an activation layer that applies an activation function to the output of the previous layer. The activation function adds non-linearity to the CNN, increasing the accuracy of the CNN; usually, real world data is non-linear. The most common

activation function is the rectified linear unit (ReLU) due to its simplicity and effectiveness. The Relu activation function outputs the input directly if the input is positive; otherwise, it returns zero.[18]

A pooling layer often follows the activation layer. The pooling layer downsamples the feature map, usually either by taking the highest value or by averaging the values. The values are taken from a small area of the feature map with a specified size that is slid across the feature map. When 2x2 max pooling with a stride of two is used, the size of the feature map is halved. [18]

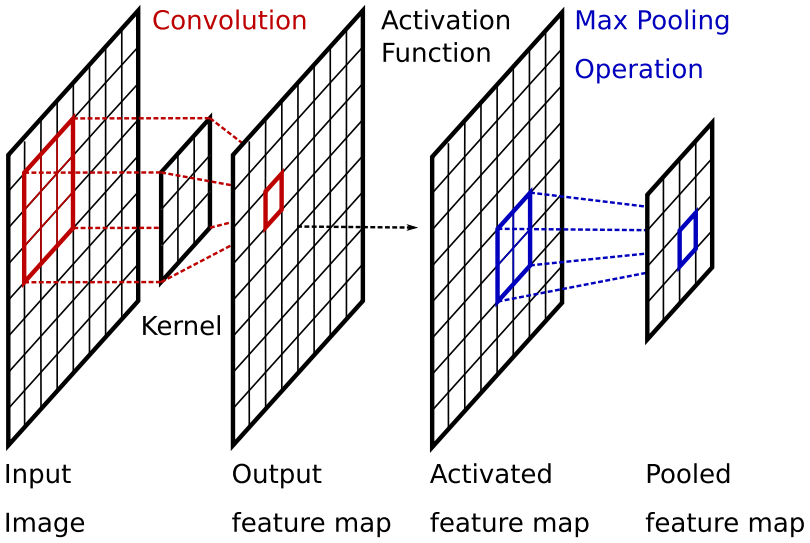

Figure 1: Basic CNN block with a 3x3 kernel size, a 2x2 max pooling, a stride of 2 and a padding of 1. [17]

Ronneberger et al. [3] proposed a CNN for biomedical semantic segmentation called U-net. A U-net was chosen as the CNN architecture used in the work presented in this thesis for its high segmentation accuracy. The U-net, shown in Figure 2, consists of a contracting path (left side) and an expansive path (right side). The contracting path consists of five convolutional blocks, each having two unpadded 3x3 convolutions followed by ReLU. The first convolutional layer has 64 feature channels, and the number of channels represents the number of learnable kernels and feature maps that the layer contains. The set of kernels is a 3D matrix called a filter. The convolutional blocks are followed by a 2x2 max pooling layer with a stride of two, which halves the spatial size of the feature map. Additionally, the number of channels is doubled.

The expansive path similarly uses double 3x3 convolutions, but the blocks are followed by 2x2 convolutions. The 2x2 convolutions upscale the feature maps, halving the number of channels.

There are skip connections (copy and crop) between the contracting path and the expansive path, as shown in Figure 2; the feature maps from the contracting path are cropped to the same size as those in the expansive path, and the information from the earlier layers is propagated to the deeper ones. The final 1x1 convolution layer is used to reduce the number of feature maps from 64 to the desired number of segmentation classes. [3]

The U-net is a fully convolutional network, meaning that it does not have a fully connected layer [3]. A fully connected layer connects all the neurons of the previous layer to the current layer, and it is usually used to produce the final output [18]. The U-net uses a 1x1 convolution layer to produce the final output. The U-net differs from other CNNs by having the expansive path with upsampling operators instead of a fully connected layer. The upsampling enables a high output resolution with high resolution features. The skip connections increase the upsampling accuracy. [3]

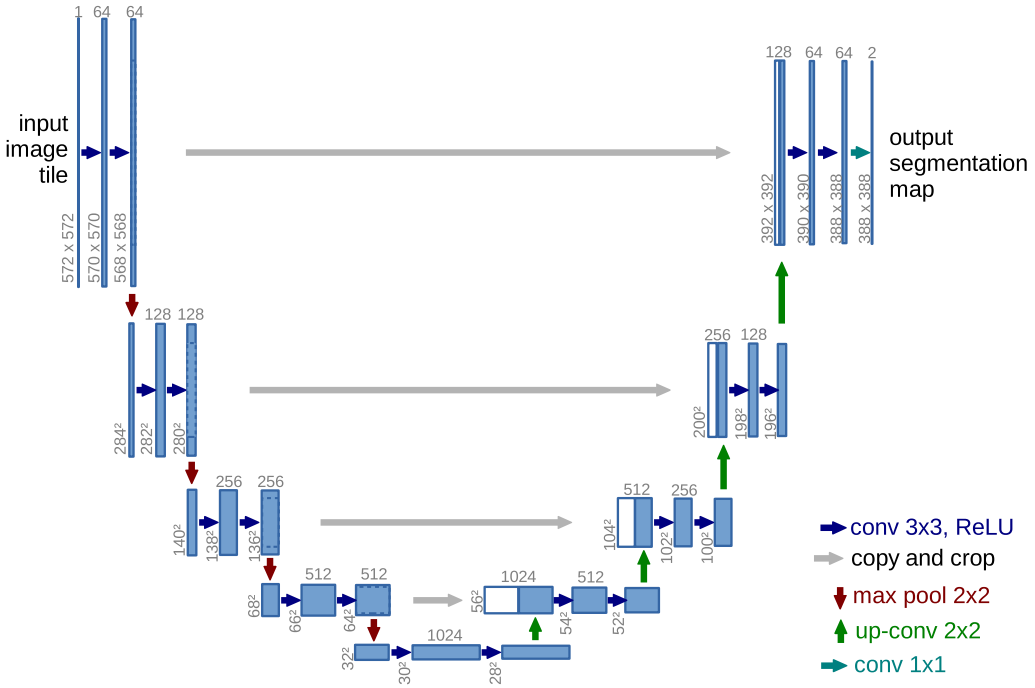

Figure 2: A U-net. The numbers represent the amount of feature channels and resolution. [3]

3 Methodology

3.1 Welding setup

The laser welding was done using an IPG Photonics YLS-10000 1070 nm fiber laser. The laser was attached, with a 300 μm optical fiber, to an IPG FLWO D50 wobble head equipped with an LDD-700 inline coherent imaging (ICI) system and a Cavitar coaxial welding camera. The laser head had a 150 mm collimator, a focal length of 400 mm, and a working distance of 348 mm, resulting in a beam diameter of 800 μm (see Figure 3). The laser head was attached to an ABB IRB 4600 6-axis articulated robot, which was used to move the laser head linearly.

The Cavitar camera was equipped with a 1.5 MP Sony IMX273 CMOS sensor. Cavitar capture software was used to operate the camera. The camera was set to 100 fps with a resolution of 720 x 540 and a mono 12 bit depth. An external pulsed laser illuminator, synced with the camera fps, was attached to the laser head. The camera was equipped with a filter that only allows light from the laser illuminator to pass.

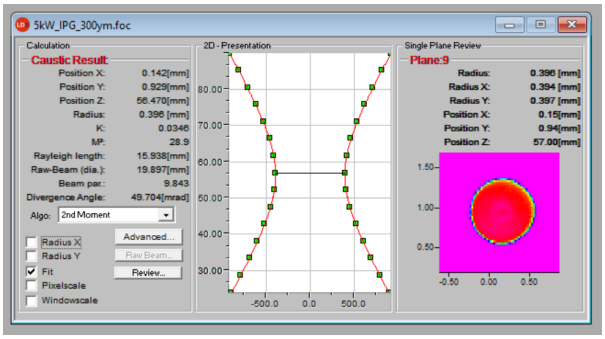

Figure 3: Laser beam profile

The workpieces were cut using a 3 kw cutting laser, with oxygen as the cutting gas, from a 4 mm SSAB E36 structural steel plate. The overall length of the workpiece was 400 mm, with a width of 125 mm. Two of these workpieces were clamped to the welding fixture table in a butt joint configuration. The workpieces were welded in two operations: first, 200 mm was welded, after which the workpiece was flipped and welded again. Each side of the workpiece had four sections with varying gaps between the butt joints. The gaps were 0 mm, 0.4 mm, 0.8 mm, and 1.2 mm in width. The workpieces were attached to a fixture table with a welding fixture. The fixture applied clamping force to the workpiece from the sides and from the top, preventing movement of the workpiece during welding.

3.2 Welding parameters

The welding was conducted using a constant laser power of 5.5 kW and with varying speeds, wobble shapes, and wobble amplitudes (see Table 1). Additionally, from previous experiments conducted at the university of Turku, the footage was used for training the U-net and was analyzed. The previous experiments were conducted with a similar setup, 5 mm Strenx 700 steel, varying laser powers and speeds, and bead on plate and butt-joint configurations.

Table 1: Welding parameters (5.5 kW)

Index	Speed (mm/s)	Frequency (Hz)	Amplitude (mm)	Wobble	Type
1	50	50	0.3	Linear	Bead on plate
2	50	100	0.3	Circle	Bead on plate
3	50	25	0.3	Eight	Bead on plate
4	50	25	0.3	Infinity	Bead on plate
11	50	50	0.4	Linear	Butt joint
12	50	100	0.4	Circle	Butt joint
21	50	25	0.4	Eight	Butt joint
22	50	25	0.4	Infinity	Butt joint
31	50	50	0.8	Linear	Butt joint
32	50	100	0.8	Circle	Butt joint
41	50	25	0.8	Eight	Butt joint
42	50	25	0.8	Infinity	Butt joint
51	40	50	0.8	Linear	Butt joint
52	40	100	0.8	Circle	Butt joint
61	40	25	0.8	Eight	Butt joint
62	40	25	0.8	Infinity	Butt joint
71	35	50	0.8	Linear	Butt joint
72	35	100	0.8	Circle	Butt joint
81	35	25	0.8	Eight	Butt joint
82	35	25	0.8	Infinity	Butt joint
91	30	50	1.2	Linear	Butt joint
92	30	100	1.2	Circle	Butt joint
101	30	25	1.2	Eight	Butt joint
102	30	25	1.2	Infinity	Butt joint

3.3 U-net

The U-net follows the original design by *Olaf Ronneberger et al.* [3] with one minor change: the padding was changed to padded to keep the spatial size the same. The model was programmed in python using PyTorch. The training was conducted for 50 epochs with a learning rate of $1 \cdot 10^{-4}$.

The loss function was the sum of Dice loss and binary cross-entropy (BCE) loss.

3.4 Dataset preparation and data augmentation

The training data for the U-net were collected from the wobble welding experiments and from previous welding experiments conducted at the University of Turku. The U-net training was started by hand drawing annotation masks for the keyholes using the CVAT Computer Vision Annotation Tool. A total of 546 annotation masks were drawn from the welding footage to train the first U-net. The training was conducted using an RTX 4070 graphics card.

The first model was used to create pseudo annotation masks from all the available footage (13344 images). From the pseudo masks, the most inaccurate masks were deleted using a python program that removed masks with small circularity, masks with either too large or too small an area, and masks that consisted of multiple areas or had holes in them. A total of 10081 masks were generated. The pseudo dataset was used to train the next U-net model. The pseudo dataset had a lower weight of 0.2 compared to the hand drawn dataset, compensating for the lower accuracy of the pseudo dataset.

The second model was used to redo the pseudo masks with increased accuracy, after which all the pseudo masks were inspected manually, and the poor ones were deleted. With sufficiently accurate masks, the images were augmented by adding noise, tilting, flipping, brightening, and increasing the gamma; each image was augmented 5 times randomly. The final dataset size for the augmented pseudo dataset was 59238, and for the augmented hand drawn dataset, it was 3276 images. This dataset was used for training the final U-net model over the course of 16 hours.

3.5 Data analysis

The trained U-net was used to detect the contours of the keyhole, as shown in Figure 4. The following features were extracted from the segmentation masks generated by the U-net using the OpenCV python library:

1. The contours of the keyhole were detected using cv2.findContours() function.

2. The area of the keyhole was measured using cv2.contourArea() function.

3. The circularity was calculated using the equation of circularity ($C = \frac{4\pi \cdot Area}{Perimeter^2}$), and the perimeter was determined by the function cv2.arcLength().

4. The radius was calculated assuming that the keyhole is round, using the equation $r = \sqrt{\frac{Area}{\pi}}$

5. An elliptic fit was performed using the cv2.fitEllipse() function.

6. From the elliptic fit, the width, length, aspect ratio, Feret diameters (x and y), and Feret diameter ratio (y/x) were calculated.

7. The root mean square error (RMSE) and the Dice score were calculated to evaluate the goodness-of-fit.

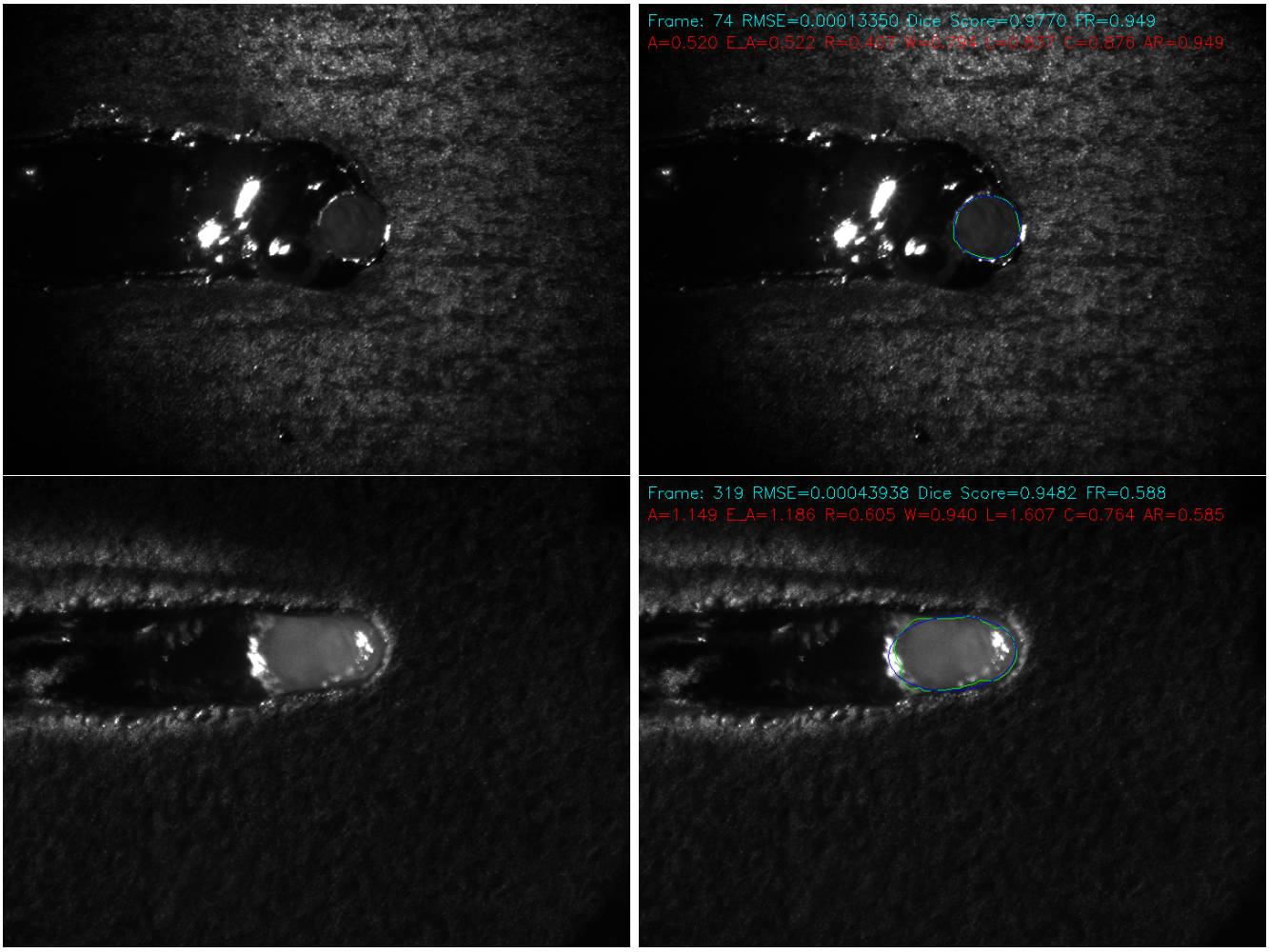

Figure 4: Keyhole segmentation. A = Area, E_A = Area of the ellipse, R = Average radius, W = Width of the ellipse, L = Length of the ellipse, C = Circularity, and AR = Aspect ratio W/L, FR = Feret ratio

4 Results

The welding was conducted using the parameters shown in Table 1, and the welding results are shown in Table 2. In Table 2, the penetration represents the depth of penetration for each section: C represents complete penetration, and I represents incomplete penetration. The amount of spatter was visually evaluated from low to high. The footage quality was evaluated based on how well the keyhole could be detected, ranging from good to poor. The poor footage quality was caused either by the blurriness of the footage or the difficulty in classifying the keyhole; the beam wobbling did not always produce a keyhole that could be accurately segmented.

Table 2: Welding results

Index	Penetration	Spatter	Footage quality
1	C	Low	Good
2	I	Medium	Fair
3	I	High	Good
4	I	Medium	Fair
11	CIII	Low	Fair
12	CIII	Low	Fair
21	IIII	Medium	Poor
22	IIII	Medium	Poor
31	IIII	Low	Fair
32	IIII	Low	Poor
41	IIII	High	Poor
42	IIII	Medium	Poor
51	IIII	Low	Fair
52	ICII	Low	Poor
61	ICII	High	Poor
62	IIII	Medium	Poor
71	IIII	Low	Poor
72	ICII	Low	Poor
81	ICII	High	Poor
82	IIII	Medium	Poor
91	IIII	Low	Poor
92	IIII	High	Poor
101	IICI	High	Poor
102	IICI	High	Poor

Due to the lack of usable footage from the wobble experiments, the footage from the previous experiments was also analyzed. To compare the keyhole images, the dimensionless aspect ratio

and Feret ratio were used (see Figure 5). Additionally, the standard deviation was calculated to quantify the change in keyhole shape. To visualize the change in keyhole behavior, a moving standard deviation (MSTD) of the aspect ratio and Feret ratio was plotted in Figure 5; the standard deviation was taken from a sliding window of 20 frames.

In Figure 5a, two distinct spikes are seen at the beginning and end. The spikes were caused by the aspect ratio being zero at the beginning and end due to the keyhole not being detected. In Figure 5a, two smaller bumps can be seen in the 5 kW MSTD curve at frame positions 210 and 380. These two bumps were caused by blurry images. In Figure 5b, It can be noted that the two bumps are not visible. Instead, the bumps in the MSTD curves are caused by sharp increases or decreases in the Feret ratio. It can also be noted that the MSTD is significantly higher for the 6 kW welding process compared to the 5 kW one.

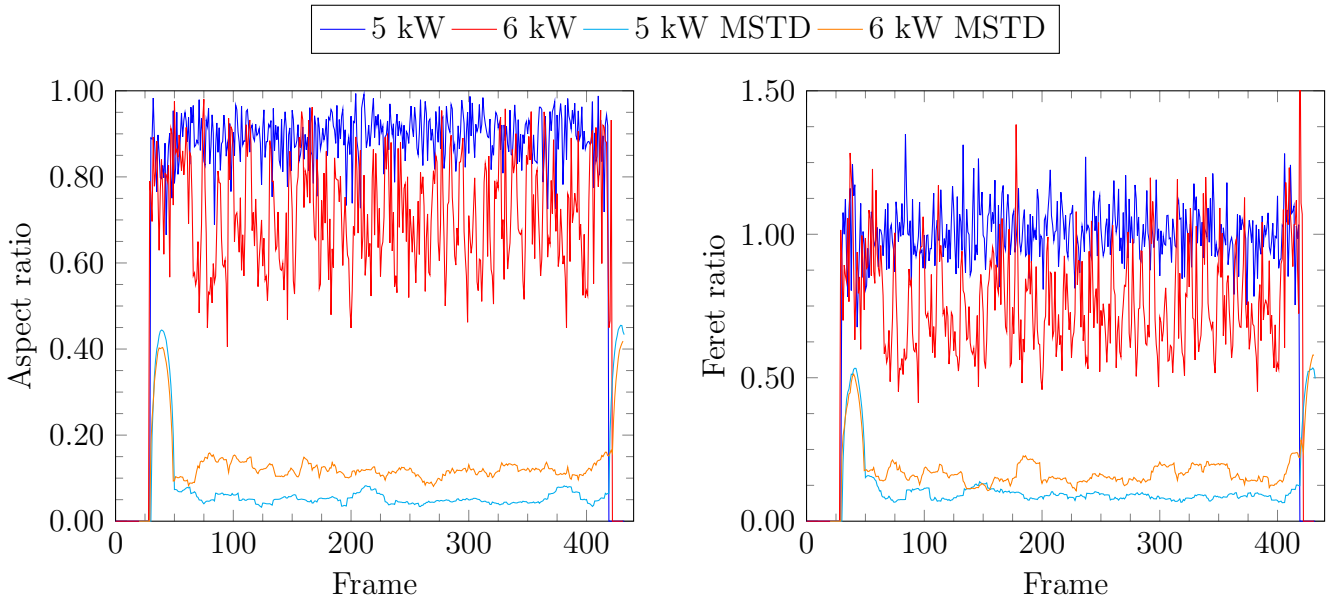

(a) Aspect ratio

(b) Feret ratio

Figure 5: Aspect ratio and Feret ratio for each frame (welding speed 50 mm/s).

The standard deviations of the measured features were taken from multiple welding recordings from frame 60 to 350; the start and end of the weld were not included. The standard deviations were plotted as shown in Figure 6. Figure 6 shows the effect that power has on the standard deviations. From the previously collected data, it was observed that the welding parameters that achieved full penetration without visual flaws in a butt joint configuration were a power of 5.2 -

5.3 kW and a speed of 46 mm/s. With a power of 5.3 kW and a speed of 50 mm/s, almost full penetration was achieved. With a power of 6 kW and a speed of 50 mm/s, back droplets were observed, caused by over-penetration. From Figure 6, it can be observed that the smallest standard deviation values are near the power that produced the best weld (5.2 - 5.3 kW).

In Figure 6, it is shown that the standard deviation of the width remains nearly constant until the power reaches 6 kW. The increase in standard deviation was caused by the highly elongated keyhole shape; the keyhole shape was no longer elliptic. This can be observed as the increase in the standard deviation of the Dice score. Since the standard deviation of the width remains nearly constant, the standard deviation of the Feret ratio represents the change in the length of the keyhole. The aspect ratio does not take the angle of the ellipse into account; hence, it can only represent the overall shape of the keyhole.

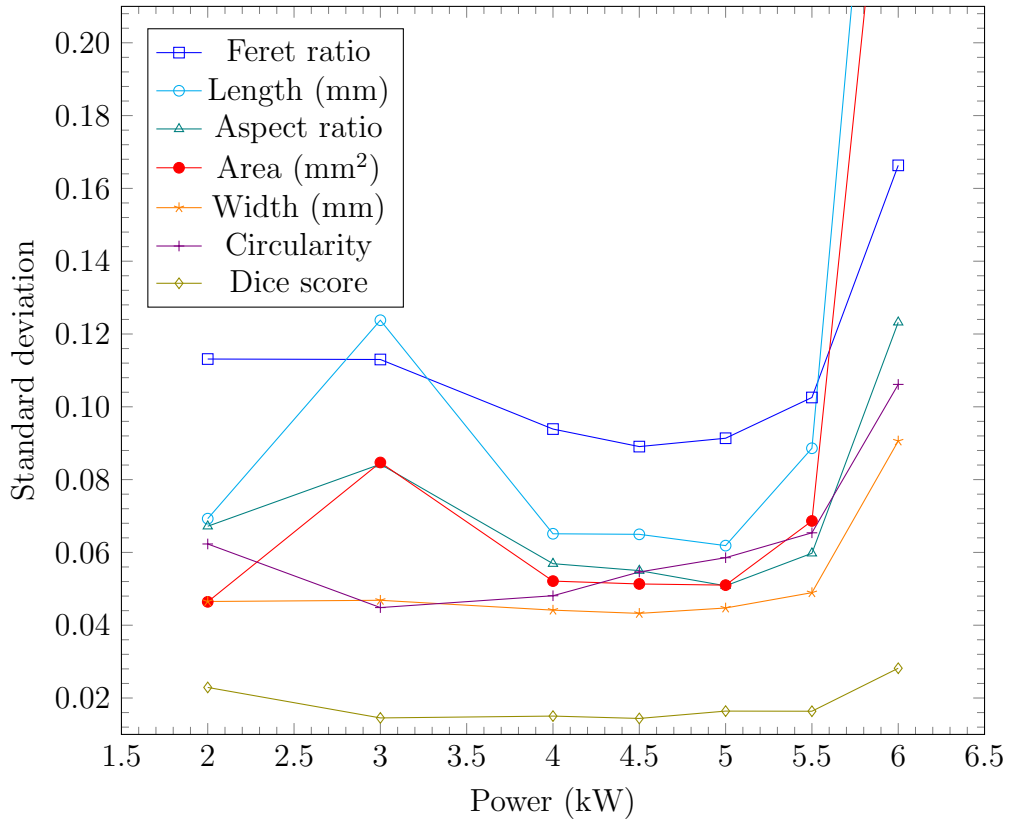

Figure 6: Standard deviations for bead on plate welds as a function of power (welding speed 50 mm/s).

For all the usable footage from the wobble experiments, a similar analysis was done: the standard deviation of the aspect ratio was calculated and plotted in Figure 7. Only the aspect ratio

was analyzed due to the beam wobbling changing the beam direction; the width and length of the keyhole are difficult to determine. The keyhole could be reliably detected only when there was no gap between the butt joint. Therefore, the footage from the bead on the plate and the first section of the butt joint with no gap was analyzed. From Table 2, It is shown that only the linear and circle patterns achieved full penetration for a welding speed of 50 mm/s. The linear pattern achieved full penetration with 0.3 mm and 0.4 mm amplitudes, and the circle with a 0.4 mm amplitude. From the figure, it can be observed that the linear pattern shows the lowest standard deviation.

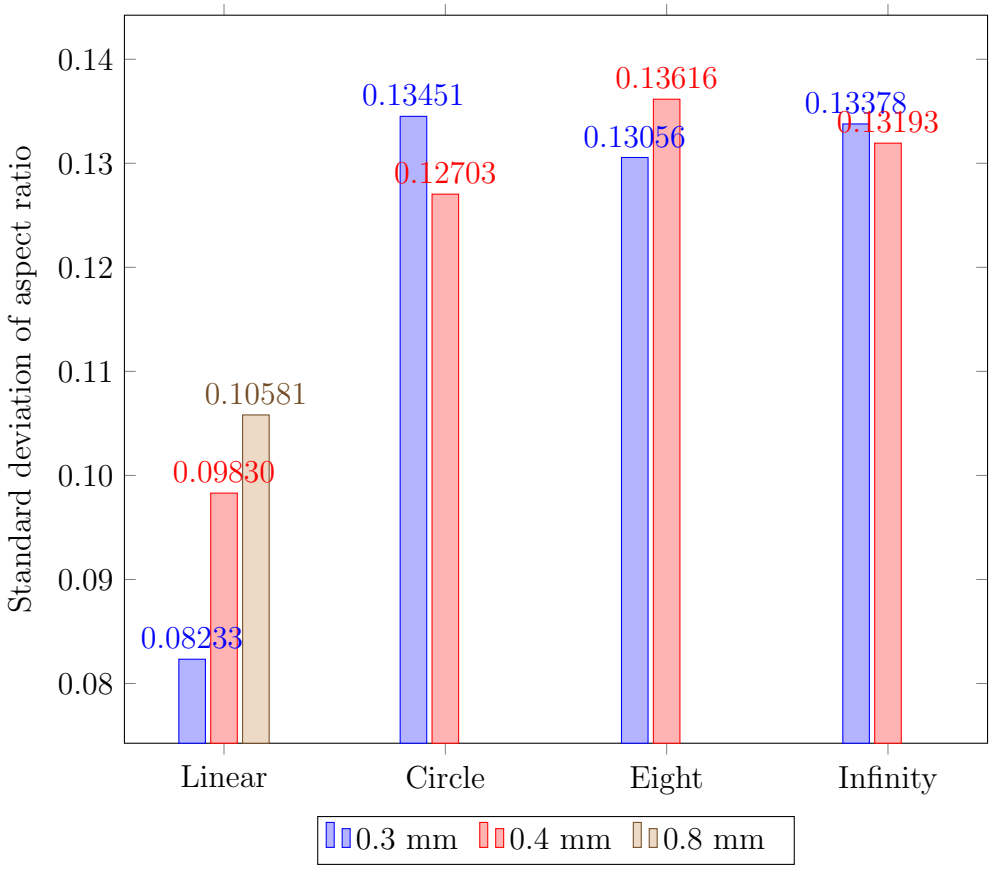

Figure 7: Standard deviation with different wobble patterns (welding speed 50 mm/s).

5 Discussion

In this thesis, the effects of laser welding parameters on keyhole dynamics were studied. A novel method of quantifying the stability of the rear wall of the keyhole was proposed: an ellipse was fitted over the keyhole images, and the standard deviation of Feret ratios was calculated. The stability of the rear wall of the keyhole plays a critical role in the formation of porosity and spatter, as discussed in Section 2.1. Figure 5b shows that MSTD can detect changes in keyhole behavior, such as the transition from an elongated to a more circular opening area. A large change in the length of the keyhole may suggest a keyhole collapse, resulting in weld defects. Figure 6 shows that keyhole stability increases near the optimal welding parameters; a stable keyhole suggests a uniform absorption of laser power, leading to high penetration.

From Figure 7, it can be observed that the standard deviation is lower for welding parameters that achieved a full penetration weld, suggesting that full penetration welds are more stable. Wobble beam welding had two major issues for coaxial monitoring: keyhole segmentation and blurriness of the image. The wobble beam keyhole image segmentation was difficult for some images due to the keyhole being challenging to classify, as shown in Figure 8. Figure 8 shows that the beam position can be clearly seen, but the keyhole is difficult to determine. The classification of the keyhole became more difficult when welding with larger wobble amplitudes, suggesting that the beam velocity is the main culprit. The wobble beam velocity might be faster than the flow of the melt pool. This would cause a jagged rear edge of the keyhole, which is challenging to classify (see Figure 8).

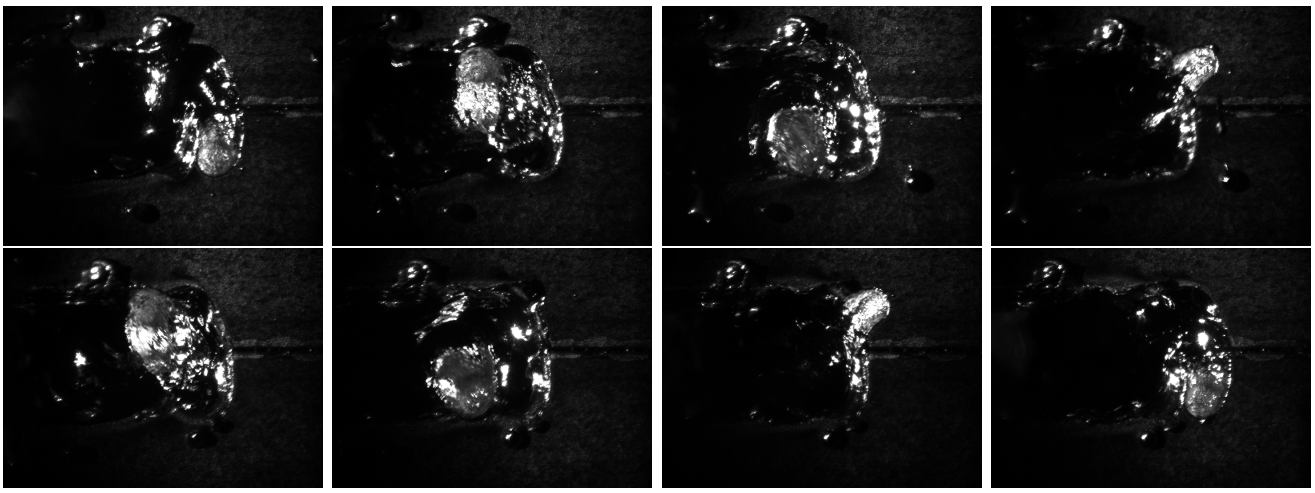

Figure 8: Eight consecutive images of welding without a clear keyhole. (Index 102)

The blurriness of the images was more prominent with welds that produced more spatter, suggesting that the blurriness might be caused by some of the following mechanisms: The excessive formation of metal vapor or a spatter globule flying in front of the field of view. The increase in metal vapor might be observed as an increased amount of spatter; the increase in vapor flow increases the amount of melt ejected. The spatter globules may instead introduce diffraction or reflective effects, resulting in image blurring. Additionally, the blurriness might be caused by the plasma plume. During wobble beam welding, the plume direction changes continuously, which can cause the plume to move into the field of view. From Figure 9, it can be seen that slight blurriness may not impact the accuracy of the keyhole segmentation significantly.

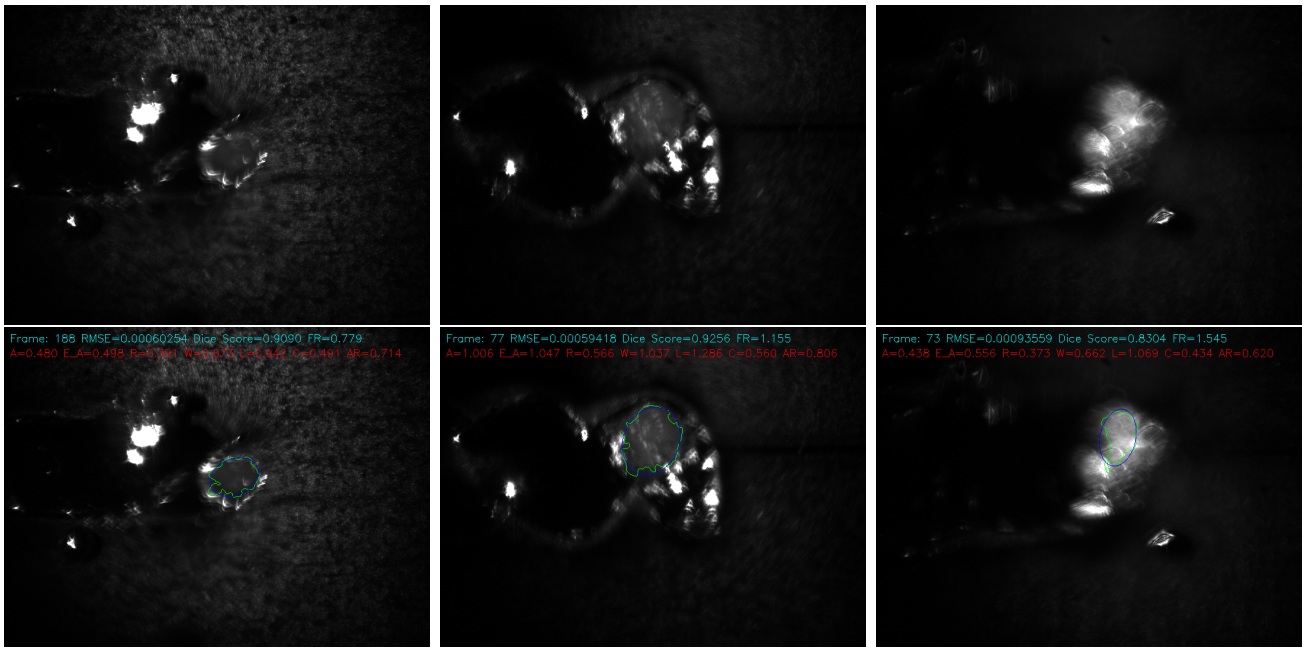

Figure 9: Blurry keyhole images from low to severe blur (Indexes 4, 42 and 41 respectively)

Compared to the other studies discussed in Section 2.2, this thesis aims to research a method to quantify keyhole stability rather than directly trying to predict the penetration or the formation of a weld defect. Other studies often analyze the frames individually; the keyhole dynamics cannot be monitored from individual frames. Even the method presented by Lu et al. [13] only uses average and mean values over the interaction time, which do not represent the change in keyhole behavior well. Some of the studies monitored the presence of a full penetration hole. From the footage used in this thesis, the full penetration hole could rarely be detected, possibly due to the curvature of the keyhole. In the images with a possible full penetration hole, the full penetration hole is

almost completely under the rear wall of the keyhole, suggesting that the curvature is hiding the penetration hole, as shown in Figure 10. It must be noted that in the images, darker areas, similar to a full penetration hole, could sometimes be detected, even if full penetration was not achieved. From this, it can be concluded that full penetration hole monitoring can only be used while welding thin metals.

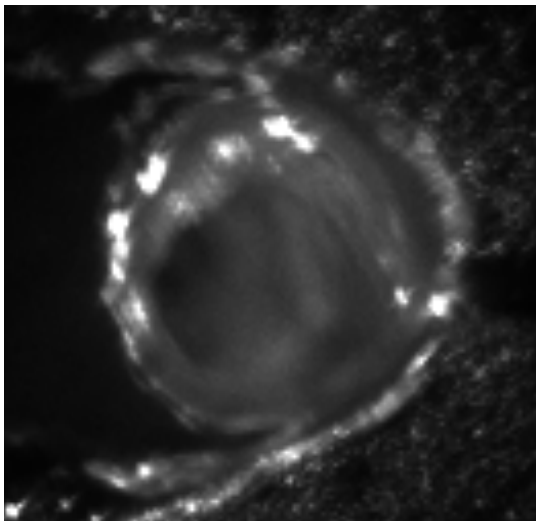

Figure 10: Possible full penetration hole

Some of the studies [15, 16] used deep-learning-based machine learning algorithms to predict penetration or weld defects. Although it has been proven that this approach works, the features extracted and the underlying keyhole dynamics remain unknown. All of the studies presented have one common problem: the defect and penetration predictions are based on welding footage that has been created with intentionally poor welding parameters. In real-world applications, highly optimized parameters are used for welding; can welding defects still be detected when the defects are not intentionally created.

5.1 Analysis of error

The monitoring method presented in this thesis has multiple sources of error. Since the monitoring method is image segmentation based, the accuracy of the segmentation masks has a significant effect on the overall accuracy of the method. In multiple keyhole images, the pixel-wise classification of the keyhole is difficult, even for a human—let alone for a U-net; the contours of the keyhole are not always sharp and easy to trace, and reflections sometimes overexpose certain areas. To combat the

inaccuracy of the segmentation masks, an elliptic fit was performed. The elliptic fit smoothed the jagged edges of the segmentation masks. The elliptic shape represents the keyhole quite well; for example, the average Dice score for parameters (46 mm/s, 5.3 kw) that achieved a full penetration weld was 0.953. It was observed that using a high welding power of 6 kw caused the formation of an elongated keyhole that was no longer elliptic; the standard deviation of the Dice score increased, and the average Dice score decreased to 0.919. Sometimes, even if the Dice score was low, the elliptic fit represented the shape of the keyhole better than the segmentation mask.

The presented coaxial monitoring method can only detect surface level changes; it might not represent the overall keyhole stability well with thicker workpieces. For a thicker workpiece, the keyhole can collapse in the middle section, which may not be visible to the camera. Additionally, sometimes the images are blurry, reducing segmentation accuracy, and the low frame rate of 100 fps does not allow for monitoring the finer movements of the keyhole.

6 Conclusions

The contours of the keyhole were successfully captured using a U-net CNN. A novel method of analyzing the data was proposed: a standard deviation and a moving standard deviation were taken from the extracted features to quantify how much the keyhole changes during welding. Data were analyzed from both wobble beam welding and welding without wobbling. The key findings can be summarized as follows:

- By taking an MSTD from the aspect ratios of the fitted ellipses, it is possible to detect changes in the overall shape of the keyhole; for example, blurry images caused bumps in the MSTD curve, which could be easily observed, as seen in Figure 5a (5 kW MSTD). The aspect ratio does not account for the orientation of the fitted ellipse and therefore cannot distinguish the length changes of the opening of the keyhole.
- The Feret ratio of the fitted ellipse can be used to detect changes in the keyhole length. The Feret ratio is smaller than one if the keyhole is elongated, and if the Feret ratio is larger than one, the keyhole opening is shorter than it is wide. The MSTD of the Feret ratio can be used to detect changes in keyhole length, as seen in Figure 5b. A sharp decrease in the length of the keyhole may indicate a keyhole collapse.
- The overall keyhole behavior was studied by taking the standard deviation of the extracted features with multiple different welding parameters. It was observed that the standard deviations were smallest near the optimal parameters, as seen in Figure 6. The standard deviation of the width remained nearly constant until the power reached 6 kW due to the keyhole shape no longer being elliptic. The shape change can be observed as an increase in the standard deviation of the Dice score and circularity. The results indicate that variation in the Feret ratio is primarily driven by changes in the length of the keyhole opening.
- The wobble beam welding shows similar behavior: the full penetration welds have the smallest standard deviations of the aspect ratio, as seen in Figure 7. The monitoring of the wobble beam was found to be significantly more difficult due to the keyhole being challenging to classify; the wobble beam velocity was too great, leading to a jagged rear edge of the keyhole and shallow penetration. This can also be seen from Table 2 as the lack of penetration for the larger wobble amplitudes.

References

[1] R. Lin, H. ping Wang, F. Lu, J. Solomon, and B. E. Carlson, "Numerical study of keyhole dynamics and keyhole-induced porosity formation in remote laser welding of al alloys," *International Journal of Heat and Mass Transfer*, vol. 108, pp. 244–256, 2017.

[2] J. Volpp and F. Vollertsen, "Keyhole stability during laser welding—part i: modeling and evaluation," *Production Engineering*, vol. 10, 09 2016.

[3] O. Ronneberger, P. Fischer, and T. Brox, "U-net: Convolutional networks for biomedical image segmentation," in *International Conference on Medical image computing and computer-assisted intervention*, pp. 234–241, Springer, 2015.

[4] D.-H. Lee, "Pseudo-label : The simple and efficient semi-supervised learning method for deep neural networks," *ICML 2013 Workshop : Challenges in Representation Learning (WREPL)*, 07 2013.

[5] T. Patterson, B. Panton, and J. Lippold, "Analysis of the laser welding keyhole using inline coherent imaging," *Journal of Manufacturing Processes*, vol. 82, pp. 601–614, 2022.

[6] R. Fabbro, S. Slimani, F. Coste, and F. Briand, "Study of keyhole behaviour for full penetration nd–yag cw laser welding," *Journal of Physics D: Applied Physics*, vol. 38, p. 1881, jun 2005.

[7] J. Volpp, "Keyhole stability during laser welding—part ii: process pores and spatters," *Production Engineering*, vol. 11, 11 2016.

[8] A. F. H. Kaplan and J. Powell, "Spatter in laser welding," *Journal of Laser Applications*, vol. 23, p. 032005, 06 2011.

[9] Cavitar, "Common welding methods and the use of laser illumination in welding imaging," *Cavitar Ltd, Application Note*, 2020.

[10] F. Abt, A. Heider, R. Weber, T. Graf, A. Blug, D. Carl, H. Höfler, L. Nicolosi, and R. Tetzlaff, "Camera based closed loop control for partial penetration welding of overlap joints," *Physics Procedia*, vol. 12, pp. 730–738, 2011. Lasers in Manufacturing 2011 - Proceedings of the Sixth International WLT Conference on Lasers in Manufacturing.

[11] C.-H. Kim and D.-C. Ahn, "Coaxial monitoring of keyhole during yb:yag laser welding," *Optics & Laser Technology*, vol. 44, no. 6, pp. 1874–1880, 2012.

[12] Y. Zhang, T. Liu, B. Li, and Z. Zhang, "Simultaneous monitoring of penetration status and joint tracking during laser keyhole welding," *IEEE/ASME Transactions on Mechatronics*, vol. 24, no. 4, pp. 1732–1742, 2019.

[13] R. Lu, H. Wei, F. Li, Z. Zhang, Z. Liang, and B. Li, "In-situ monitoring of the penetration status of keyhole laser welding by using a support vector machine with interaction time conditioned keyhole behaviors," *Optics and Lasers in Engineering*, vol. 130, p. 106099, 2020.

[14] A. Aminzadeh, S. S. Karganroudi, N. Omidi, N. Barka, and A. E. Ouafi, "Data-driven porosity monitoring in aluminum laser welding: integration of high-speed imaging and machine learning," *Optics & Laser Technology*, vol. 195, p. 114545, 2026.

[15] B. Zhang, K.-M. Hong, and Y. C. Shin, "Deep-learning-based porosity monitoring of laser welding process," *Manufacturing Letters*, vol. 23, pp. 62–66, 2020.

[16] H. H. Núñez, L.-W. Hsu, K. S. Ribeiro, A. Salminen, and W. M. Bessa, "In-situ monitoring and online prediction of keyhole depth in laser welding by coaxial imaging," *Procedia CIRP*, vol. 124, pp. 793–796, 2024. 13th CIRP Conference on Photonic Technologies [LANE 2024], 15-19 September 2024, Fürth, Germany.

[17] T. Georgiou, Y. Liu, W. Chen, and M. Lew, "A survey of traditional and deep learning-based feature descriptors for high dimensional data in computer vision," *International Journal of Multimedia Information Retrieval*, vol. 9, no. 3, pp. 135–170, 2020.

[18] M. Krichen, "Convolutional neural networks: A survey," *Comput.*, vol. 12, p. 151, 2023.